frontiers | Frontiers in Astronomy and Space Sciences

TYPE Original Research
PUBLISHED 25 June 2025
DOI 10.3389/fspas.2025.1613164

OPEN ACCESS

EDITED BY
Larry Lyons,
University of California, Los Angeles,
United States

REVIEWED BY
Rajan Itani,
University of Alaska Fairbanks, United States
Garima Malhotra,
University of Colorado Boulder, United States

*CORRESPONDENCE
Anneliese L. Schmidt,
als53@njit.edu

RECEIVED 16 April 2025
ACCEPTED 06 June 2025
PUBLISHED 25 June 2025

CITATION
Schmidt AL, Meriwether JW, Cooper MB, Gerrard AJ, Goodwin LV, Zhang S-R and Ye Y (2025) Detection of wave activity in measurements of thermospheric vertical winds and temperatures at subauroral latitudes.
Front. Astron. Space Sci. 12:1613164.
doi: 10.3389/fspas.2025.1613164

Detection of wave activity in measurements of thermospheric vertical winds and temperatures at subauroral latitudes

Anneliese L. Schmidt[1]*, John W. Meriwether[1], Matthew B. Cooper[2], Andrew J. Gerrard[1], Lindsay V. Goodwin[1], Shun-Rong Zhang[3] and Ying Ye[4]

[1]Department of Physics, Center for Solar-Terrestrial Research, New Jersey Institute of Technology, Newark, NJ, United States, [2]Orion Space Solutions (An Arcfield Company), Louisville, CO, United States, [3]Haystack Observatory, Massachusetts Institute of Technology, Westford, MA, United States, [4]Department of Physics and Astronomy, Rice University, Houston, TX, United States

The need for high precision measurements of vertical winds with uncertainties on the scale of 3–5 m s^{-1} and a temporal cadence of 1–2 min to achieve detection of gravity wave (GW) structure has made it exceedingly difficult to study the response of the thermosphere to the propagation of GW activity. Herein we present subauroral, midlatitude thermospheric wind and temperature observations using redline 630 nm measurements obtained with a 15 cm narrow field Fabry-Pérot Interferometer (FPI), named the Hot Oxygen Doppler Imager (HODI). These measurements were obtained in a first light campaign at Jeffer Observatory (41.03°N, 74.83°W) located in Jenny Jump State Forest in northwestern New Jersey. The heightened sensitivity of HODI enables analysis of observations with uncertainties of approximately 3–5 m s^{-1} for vertical wind speeds and 10–15 K for temperatures for 2-min exposures. Data was collected during periods of both geomagnetically quiet and active conditions, and GW structures were seen in both data sets. One detailed observation, taken the night of 25 July 2022, enabled the ≈90° phase shift between vertical winds and temperatures to be inferred, as per standard GW polarization relations with weak viscous dissipation. However, most other observations are found to have little correlation between the two series of temperature and vertical wind. We interpret this to be a result of the propagation and interaction of multiple GW events superimposed upon one another. Wave-like structures in the ionosphere observed in differential total electron count maps, or traveling ionospheric disturbances (TIDs), are often related to GW induced processes, and we provide comparisons of selected wave events observed by HODI to TIDs. These results suggest in a general sense that a relationship may exist between wave fluctuations seen in both the neutral atmosphere and the ionosphere. However, we suggest that the 35–70 km vertical extent of the 630 nm nightglow layer combined with an environment of multiple GW events with differing propagation speeds and vertical wavelengths may have the effect of diminishing or eliminating possible existing temperature and vertical wind correlation.

KEYWORDS

aeronomy, airglow, gravity wave, vertical winds, thermosphere

1 Introduction

Lower-boundary driving wave activity in the upper atmosphere, signified by perturbations of the thermospheric winds and temperatures, is an indication of energy transfer from lower altitudes into the thermosphere. Such activity has been suggested to trigger ionospheric instabilities within the coupled ionosphere/thermosphere system (Hines, 1960; Huang et al., 1994; Nicolls and Kelley, 2005). Studies of thermospheric winds utilizing Doppler velocity measurements of the 630 nm OI spectral profile during periods of low and high geomagnetic activity were first reported by Biondi and Feibelman (1968), Armstrong (1969), and Hays et al. (1969). Fabry-Perot interferometers (FPIs) have been extensively used since then to measure line-of-sight (LOS) Doppler velocity measurements in the cardinal and zenith directions to derive the thermospheric wind vector U (u,v,w). Data representing FPI observations of thermospheric vertical winds have been studied, with notable results demonstrating large apparent vertical winds evident during enhanced geomagnetic activity (Hernandez, 1982; Sipler et al., 1995) and at midlatitudes (Larsen and Meriwether, 2012) with oscillatory behavior (Hernandez, 1982; Sipler et al., 1995; Innis and Conde, 2001; Trinh et al., 2018)) that have been identified to be caused by the existence and ubiquitous nature of gravity waves (GWs) in the thermosphere (Hines, 1960). Wind and temperature oscillations and wave structures caused by GW activity are diminished by the viscous dissipation in the thermosphere which can dampen wave activity.

Traveling ionospheric disturbances (TIDs) are characterized by quasi-periodic, spatially propagating wave-like structures in the F-region plasma. Medium-scale TIDs (MSTIDs) are commonly observed in 630 nm OI nightglow imagery with having systematic westward and equatorward motion at nighttime in the Northern Hemisphere (Shiokawa et al., 2009; Martinis et al., 2009; Otsuka et al., 2013). These events can be identified via perturbations of the spatial distribution of time-differenced, i.e., differential, total electron count (dTEC) maps. MSTIDs were originally explained as being a consequence of the Perkins instability as the predicted propagation direction is consistent with the observed southwestward direction (Perkins, 1973). However, the shortcoming of this explanation is that the growth rate of the Perkin's instability was found to be much slower than what is apparent in observations. Moreover, a seeding mechanism would also be required (Kelley and Makela, 2001). Kelley and Fukao (1991); Shiokawa et al. (2003); Nicolls and Kelley (2005); Makela and Otsuka (2012) among others have speculated that GWs could induce polarization electric fields which would reinforce the growth rate of Perkin's Instability. Zhang et al. (2021) used dTEC maps and incoherent scatter radar data and found evidence suggesting periodic meridional polarization electric fields that might be associated with midlatitude GW events. MSTIDS and large-scale TIDs (LSTIDs) are often classified as having a close relation to induced activity from propagating and dissipating GWs. Disturbed neutral winds associated with the propagation of GWs create and/or enhance electric fields, transferring energy and momentum from the F-region plasma to the upper atmosphere, thus contributing to the high complexity of the coupling between the thermosphere and ionosphere.

It has been nearly impossible to study the response of the thermosphere due to GW activity in the past due to the need for high precision Doppler velocity measurements on the scale of 3–5 m s^{-1} for winds and a cadence of 1–2 min to successfully detect GW events. Ford et al. (2007) was able to observe wave activity from 630 nm OI emissions in high latitude thermospheric winds at very fast cadences (≈15s) and observed waves with very high periodicity (14 min to several hours). Unless the instrument etendue is adequate to achieve the detection of the small changes in the vertical wind speed and temperature expected for GW activity, studying the dynamic behavior of these fine structures for the thermosphere zenith region at midlatitudes becomes exceedingly difficult. In this paper we present results with standard errors typically 3–5 m s^{-1} for line-of-sight (LOS) winds and 10–15 K for temperatures for a 2 minute exposure time. This level of high precision has been achieved using the Hot Oxygen Doppler Imager (HODI), a 15 cm diameter FPI, that has a capability of imaging a 12 ring interference pattern for the 630 nm OI emission. This paper presents FPI data representing observations of the variations of wind and temperature that are interpreted to be caused by GW events. We also present examples of simultaneous observations of dTEC variations that are generally associated with GW events.

2 Instrumentation

HODI is a 15 cm aperture etalon FPI that uses an apochromatic lens assembly with four elements and focal length of 300 mm developed by Keo Scientific, Ltd. This optical component provides the correction needed to achieve a fully focused ring pattern on the charge coupled detector (CCD) chip within the focal plane (Unick et al., 2019) that includes 12 and 11 rings for OI 630 nm and OII (O^+) 732 nm emissions, respectively. The etalon plate separation is 1.4925 cm which was chosen to blend the two lines of the O^+ (2P-2D) doublet into superposition within one order at this high resolution. HODI has a three-degree field of view with a double axis periscope (Skyscanner) that allows for the optical field of view to be directed toward any spot in the sky as well as downward toward the calibration port window. This instrument uses a 1024 × 1024 pixel array mounted on an Andor CCD with a dark noise of 0.0001 counts/sec or better for the cooler temperature of ≈ − 80°C. A binning of 2 × 2 was chosen for observations as this reduces the readout noise impact upon the observations.

The low noise CCD camera has a 90% imaging quantum efficiency. Moreover, the field of view of each of the 12 rings is the equivalent of the field of view of a single order scanning FPI such as that discussed extensively by Hernandez (1986). With a 15 cm etalon aperture, HODI has an increased field of view of ±2.5° relative to a single order scanning FPI. The HODI optics also collect light over the full order continuously rather than partially using an aperture that passes only 10% of a full order at any one time. Taking all of the instrumental gains in sensitivity (12 orders rather than one, 90% quantum efficiency rather than the nominal 10% for a GaAs photomultiplier, and the factor of eight represented by the continual staring at the interference pattern rather than partially (through an aperture)) into consideration, HODI has a total increased sensitivity gain of a factor of approximately 900 when compared to that of a gap

scanning FPI. This heightened sensitivity of HODI allows a search for possible GW behavior and events with a standard error typical of 3–5 m s^{-1} for zenith wind speeds and 10–15 K for temperatures for 2 minute exposures.

The analysis of FPI images to extract wind and temperature measurements from FPI data is based upon the implementation of the profile fitting analysis described by Harding et al. (2014). This approach is based upon first determining the ring center position followed by performing an annular summing of the 512 × 512 superpixel signals about the ring center as described by Coakley (1995) to determine a one-dimensional interferogram with 500 points along the abscissa with 42 points per order at 630 nm. The FPI instrument function at the 630 nm emission wavelength is calibrated using a frequency stabilized HeNe 632.8 nm laser source. The position of the ring center is determined by analyzing cross-sections of the observed image to generate the interferogram. The two peaks of the innermost order relative to the ring center were determined for a Gaussian function and the ring center pixel coordinates were averaged using all of the cross-section estimates of the ring center position. Once the peak ring center is calculated and the 1D interferogram is generated, the temperature derived from the Doppler broadening of the FPI instrument function and the intensity determined from the area covered by the 1D spectral profile can be derived by using a non-linear least square fitting procedure (Innis et al., 1999; Meriwether et al., 2011; Shiokawa et al., 2012; Nicolls et al., 2012; Harding et al., 2014).

The calculation of the Doppler zero assumes that the averaged amplitudes of the zenith wind speed over long periods of time is small relative to the horizontal speeds. Using this assumption, the Doppler zero was found using the average of all of the phase differences between the 630 nm zenith peak and the laser peak positions. The HODI analysis algorithm follows the methods outlined in Harding et al. (2014). The Harding et al. (2014) blurring model is used to fit the interferogram peaks under the assumption that some vignetting is causing the peak height to decrease slightly and the instrumental width to broaden somewhat. The usage of a non-linear Airy function with optical distortion parameters as the instrument function allows for the best estimate of accurate wind velocities. The retrieval of the error estimates for the HODI data products is also outlined in Harding et al. (2014). The error bars plotted in this study, derived from the Harding analysis algorithm, represent an accurate measure of the retrieval error in carrying out the non-linear least-square fit of the model spectral profile to the data. The error bars of the HODI measurements do not follow a statistical random fluctuation pattern associated with the randomness of noise. This supports our view that the results of this study are true wave patterns and not the products of noise.

One concern regarding the analysis of 630 nm observations using HODI is whether the 1.0 nm passband of the 630 nm filter is sufficient to remove or attenuate the weak OH contamination present at 627.9 nm. Recent work by Kerr et al. (2023) has demonstrated that the existence of this OH emission will introduce an error in the Doppler shift and Doppler broadening retrieval of the LOS wind velocities and the temperature derived from the comparison of the forward model to the data. While the OH emission does represent a possible source of error, we suggest that it is not serious, as the 630.0 nm emission rate is high during the near solar-maximum period, with our data sets being taken in Summer 2022. Filter fabrication technology has improved such that more narrow bandwidth filters may be used to help ameliorate this concern in future measurements in new instrumentation. The OH contamination concern is further discussed in Section 3, Section 4, Section 5.

The first-light campaign using the HODI instrument took place at the Jeffer Observatory (JO) located in Jenny Jump State Forest in northwestern New Jersey (41.03°N, 74.83°W). The observation period extended from late July to late September 2022.

3 Observations

During its first light campaign at JO, HODI observed the 630 nm emission profile in the zenith and cardinal directions with an exposure time of 120 s for each direction. In this study, only the zenith direction was used in the analysis. Only observing nights with clear skies were processed using the data analysis procedure discussed in Section 2. We present perturbations and wave activity in the vertical winds, w, as well as the residual vertical wind w' which is the result of the subtraction of a high-order polynomial fit w_0 from w. We also present these perturbations for the residuals of the temperature observations T′ from the subtraction of a high-order polynomial fit T_0 from T. Herein, the oscillations and wave structures are quantitatively defined based on the Brunt-Väisälä period which is roughly 15 min in the thermosphere. In this study, long-term periodicity of a wave is defined as a periodicity that is considerably longer (2–4 h) than the Brunt-Väisälä period, and a high frequency wave structure is defined as being near but less than the Brunt-Väisälä frequency. Conversely, a low frequency GW event is one with a period that is much longer than the Brunt-Väisälä period.

We highlight one series of observations showing evidence of a monochromatic wave event. In this study, monochromatic is used to describe a wave event in which the wave is spatially and temporally coherent, with an apparent wavelength. In addition, from a total database including measurements over 57 nights, we selected two sets of five nights, each with respect to high or low geomagnetic activity. We will use these results to showcase HODI observations of vertical wind and temperature wave activity in subauroral latitudes and to determine what effects on thermospheric dynamics might develop as a result of increased geomagnetic activity. We conclude with the presentation of a case study of two nights of activity selected from these observations that also include dTEC maps generated at MIT Haystack Observatory using GNSS TEC data. The data includes observations from both the GPS and GLONASS constellations. The dTEC values are obtained by detrending the smooth background TEC variations using 30-min sliding windows (Zhang et al., 2017c; Zhang et al., 2017a) and have been used extensively for studying the effects of TIDs. We present dTEC and potential TID activity as an insight into the ionosphere during congruent observations from HODI, as one-to-one comparisons between wind or temperature fluctuations do not appear to agree with respect to dTEC observations at the location of JO.

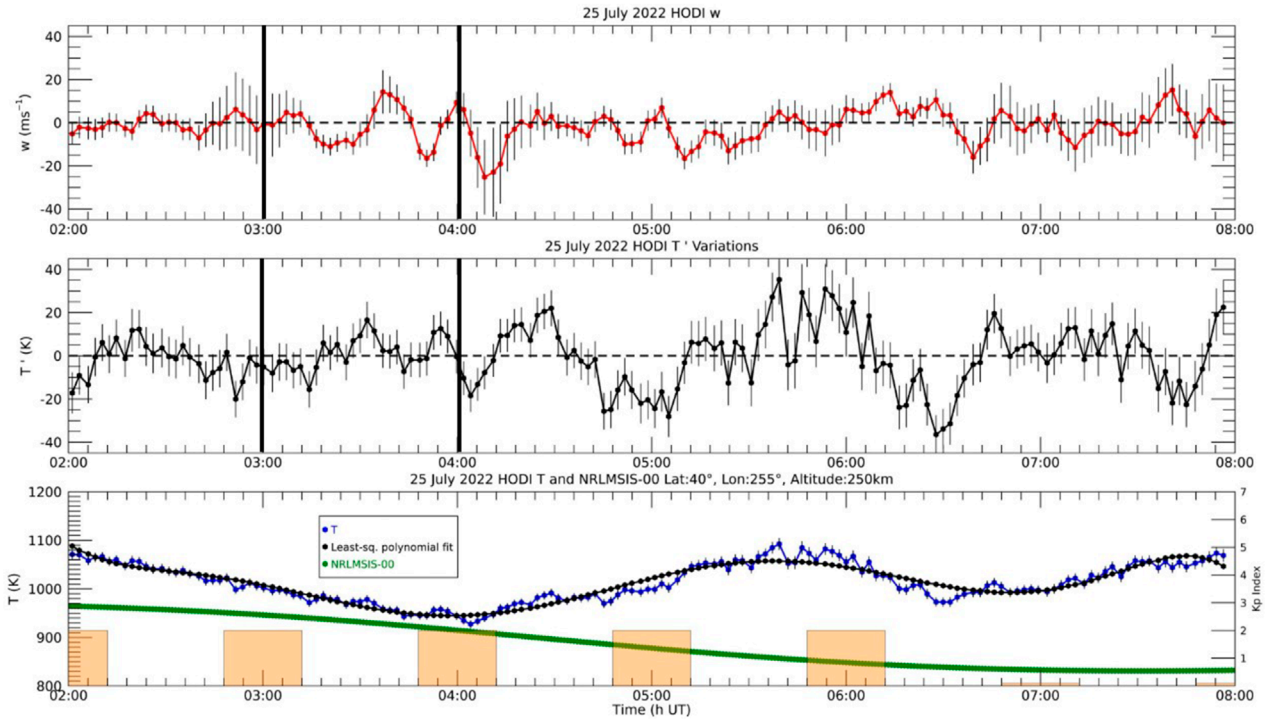

FIGURE 1
HODI observations of vertical winds (top, w) and residual temperatures (middle, T ′) from the subtraction of the observed temperatures (bottom blue, T) from the high order least-square polynomial fitting (bottom black) with the NRLMSIS-00 empirical model with inputs of altitude: 250 km, Lat.:40°, Long.: 255° (bottom green, T) and approximate Kp index (bar graph). The bolded vertical lines at 03:00–04:00 UT indicate the range of time used in the Hodogram in Figure 2.

3.1 Potential monochromatic wave event on 25 July 2022

The wind and temperature measurements of the HODI 630 nm emission profiles highlight potential monochromatic GW fluctuations in the vertical wind and temperature on 25 July 2022 shown in Figure 1. The skies above JO were clouded in the early evening (02:00–05:00 UT), but wave fluctuations were picked up by HODI nonetheless. Moderate cloud cover can lightly attenuate measurements observed by HODI, which did not greatly affect the data products used in this study. The vertical winds show a $\approx \pm 15$ m s^{-1} fluctuation around 03:30–04:00 UT with small amplitudes relative to nights with active geomagnetic conditions and wave structure with long-term periodic behavior after the initial fluctuation. Error bars larger than the amplitudes of the vertical wind oscillations are apparent around 03:00 UT and periodically after 04:00 UT, but the respective error bars during the speculated GW event at 03:00–04:00 UT are much less than the amplitudes of the vertical wind and temperature fluctuation data.

The raw temperature observations were fitted via a high-order least-square polynomial fit and the residual temperatures were derived from the difference of the raw and fitted temperatures and are plotted in Figure 1. The Kp index for each hour of observations are plotted against the temperature measurements to show the current geomagnetic conditions, as well as the neutral temperatures from the NRLMSISE-00 empirical model (Picone et al., 2002) to show thermal variations of the thermosphere temperature at 250 km and at the approximate latitude and longitude of JO. Kp index was used to highlight the general level of geomagnetic activity that may affect the thermosphere. Wave fluctuations in the temperature residuals on the order of $\approx \pm 30K$ can be seen starting roughly after 04:00 UT. We see more activity in the residual temperatures during the period of heightened Kp indices from 04:00–06:00 UT. Visual inspection suggests the appearance of wave structure in vertical winds and residual temperatures near 03:30 UT.

Figure 2 shows the phase differences between the residual temperature series and the vertical wind oscillation series using a hodogram graphic. Data selected for the period from 03:00–04:00 UT, the time of the proposed monochromatic GW event, is shown in Figure 2 with the residual temperature and vertical wind velocity presented as the abscissa and ordinate, respectively. A circle is created in a hodogram when the temperature residuals leads the vertical winds by a phase angle of 90°. A phase lead with the temperatures leading the vertical winds by ≈90° is consistent with the expected behavior of GWs affected by weak viscous dissipation as discussed by Pitteway and Hines (1963); Nicolls et al. (2012); Vadas and Nicolls (2012) among others. By visual inspection, the 25 July 2022 hodogram plotted for the period of 03:00–04:00 UT has a circular appearance but is slightly misshapen which we suggest is caused by viscous dissipation in the thermosphere.

A keogram (composite of meridional cross-sections) was utilized to examine the dTEC of the approximate location of JO (41.03°N) changing with time on 25 July 2022 in Figure 3. Minor

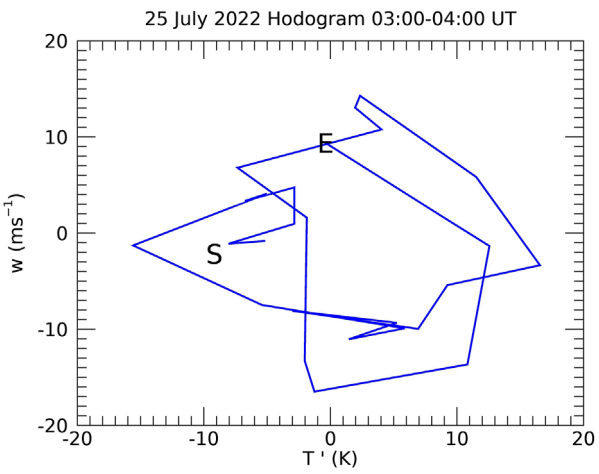

FIGURE 2
Hodogram from HODI residual temperature (T ′) observations and vertical wind velocities (w) from 25 July 2022 from 03:00–04:00 UT. S marks the start of the observations at 03:00 UT, E marks the end of the observations at 04:00 UT.

elevated values of dTEC are visible from 03:00–04:00 UT, but there are evident prevailing poleward TIDs throughout the evening across ≈41°N latitude showing signatures of background TIDs that were propagating throughout the night across JO. Further discussions regarding the HODI GW observations are in Section 4.

3.2 Active and quiet geomagnetic observation wave analysis

We conducted case studies of vertical wind velocity and temperature observations for a selection of geomagnetic active and quiet nights observed by HODI. Clear skies prevailed for these nights except for the duration of the observation period (02:00–09:00 UT) at JO on 26 August 2022 which was partly cloudy. These dates were chosen based on a review of both weather and Kp-indices. The nights with the best clarity as well as the highest and lowest series of Kp indices were chosen for this case study.

Figures 4, 5 present the vertical wind velocities and temperatures observed by HODI for active and quiet geomagnetic nights between 02:00 and 09:00 UT, respectively. These plots include a comparison of wave structure as seen in the vertical wind velocity data and in the temperature residual data observed by HODI. Also included in this graph is the NRLMSIS-00 model curve and Kp index as explained prior. A high-order least-square polynomial fit was used in the calculation of the temperature residuals to probe the high-frequency wave patterns in the raw temperature data. Since the vertical winds have a precision good enough to see high frequency wave structure, the polynomial fit is utilized to demonstrate low frequency, long term periodic behavior of the vertical wind activity.

The dates of nights selected for the case study of active geomagnetic nights observed by HODI include 19, 30 August and 3, 9, 27 September 2022. Inspection of these results show both high and low frequency wave structure in all active vertical wind velocity observations except for 3 September 2022 which was quite a bit less dynamic in spite of the background enhanced geomagnetic activity. Error bars are much less than the amplitudes of the vertical winds and temperature oscillations for all of the selected nights except for 3 September 2022, highlighting that the oscillations are unlikely due to noise. 19 August 2022 observations by HODI showcase high frequency oscillations in the vertical winds on the scale of ≈ ± 15m s^{-1}. The series of residual temperatures show lower frequency oscillations with wave behavior that seems to have no discernible qualities relative to amplitude or period. A similar example is seen for the 27 September 2022 observations with an additional increase in temperature to ≈1300 K around 06:00 UT. The two nights of 3 September and 9 September 2022 feature low temperatures in spite of the high Kp index with similar slight wave fluctuations in the residual temperatures. However, 9 September 2022 contains low frequency wave behavior in the vertical winds with respect to the 8 hour period of observations, while the 3 September 2022 vertical winds contain none. The large increase in temperature as well as the high amplitude vertical wind observations on 30 August 2022 will be discussed in further detail in Section 3.2.1.

The case study based on quiet geomagnetic nights observed by HODI includes dates 14, 24, 25, 26 August and 2 September 2022. In these results, the error bars are much less than the amplitudes of the temperature oscillations for all of the selected nights, but the vertical wind data show fluctuations of similar magnitude to the error bars. Little low frequency wave structure are noted in any of these nights of data, but some high frequency oscillations are prevalent with little discernible pattern in period or amplitude. Some vertical wind wave structure can be seen in the observations from 25 August 2022 around 07:00 to 09:00 UT with amplitudes ≈ ±10m s^{-1}. The residual temperatures, on the other hand, vary greatly in wave activity. 24 August and 26 August have temperature oscillations with amplitudes of ≈ ±40K that look to be similar to that of a wave train series, while 14, 25 August and 2 September have features of oscillations with amplitudes ≈ ±20K and irregular periodicities, with little discernible structure. The oscillation with a period of roughly 2 hours in the temperature residuals on 26 August 2022 will be discussed in further detail in Section 3.2.2.

3.2.1 30 August 2022 active wind and temperature wave structures

One night of interest from the active geomagnetic and clear nights is 30 August 2022 as shown in Figure 6. There is a temperature spike of from ≈1,000–1,300 K peaking around 06:00 UT. This follows a similar trend as the increase in Kp-index where the increase in raw temperature starting around 04:00 UT is also approximately when the Kp index increases from two to four. Wave structures in the residual temperature data are apparent with peaks that are nearly 2 hours apart. From 03:00 to 08:00 UT, an oscillation with a period of 5 hours is visible in the vertical wind data. The amplitudes for these wave structures are larger than their respective errors at the time of fluctuation. The assumption that the averaged amplitude of the vertical wind measurements is zero over long periods of time was tested and clarified by excluding the largest upward vertical wind data from the average. The corrected vertical winds showed only a very modest reduction in the speeds (≈ −2m s^{-1}). This test revealed that no correction to the average vertical was needed, and the vertical winds were left without any adjustment due to these results.

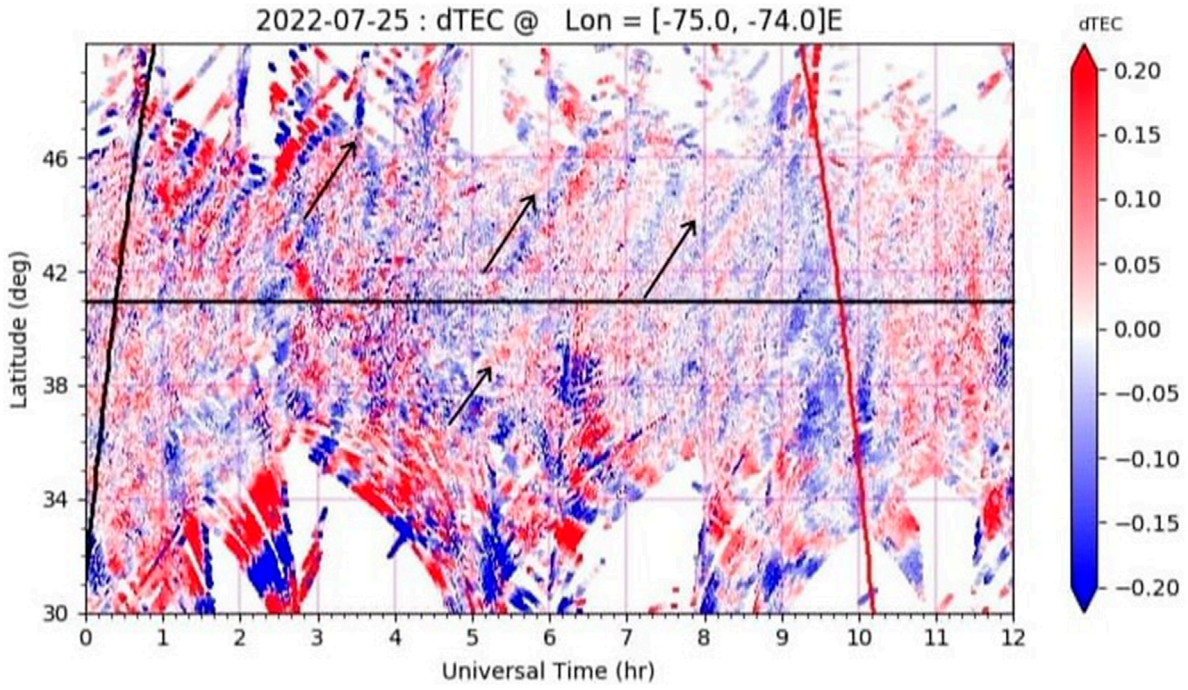

FIGURE 3
dTEC between −75° and −74° east longitude for approximate location of JO (41.03°N, 74.83°W) with varying latitudes and times on 25 July 2022 with a horizontal black line at 41°N. Tilted vertical black and red lines represent the sunset and sunrise terminators, respectively. The black arrow indicates direction of propagation in the meridional direction.

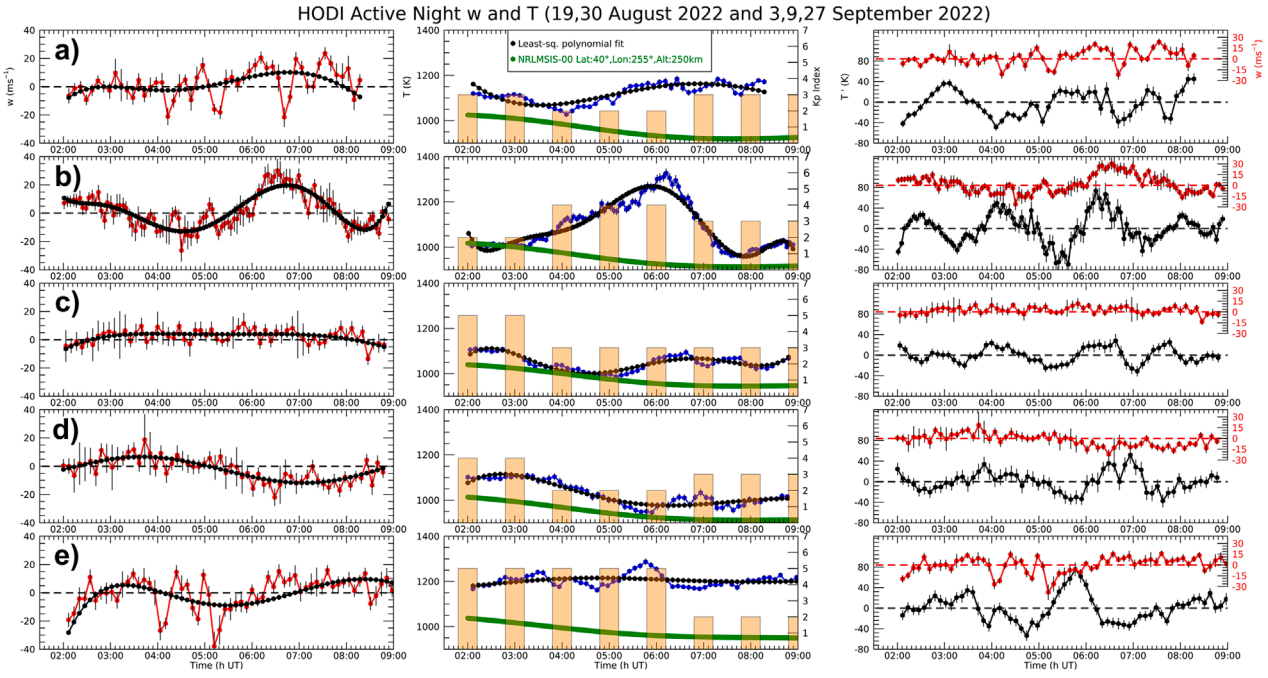

FIGURE 4
Comparison of vertical winds (red, w) and temperature residuals (right black, T ′) measured by HODI derived from the subtraction of observed temperatures (middle blue, T) from the least-square polynomial fitting (middle black) for the dates: **(a)** 19 August 2022, **(b)** 30 August 2022, **(c)** 3 September 2022, **(d)** 9 September 2022, **(e)** 27 September 2022. Temperatures are plotted with the NRLMSIS-00 empirical model with inputs of altitude: 250 km, Lat.:40°, Long.: 255° (bottom green, T) and approximate Kp index (bar graph).

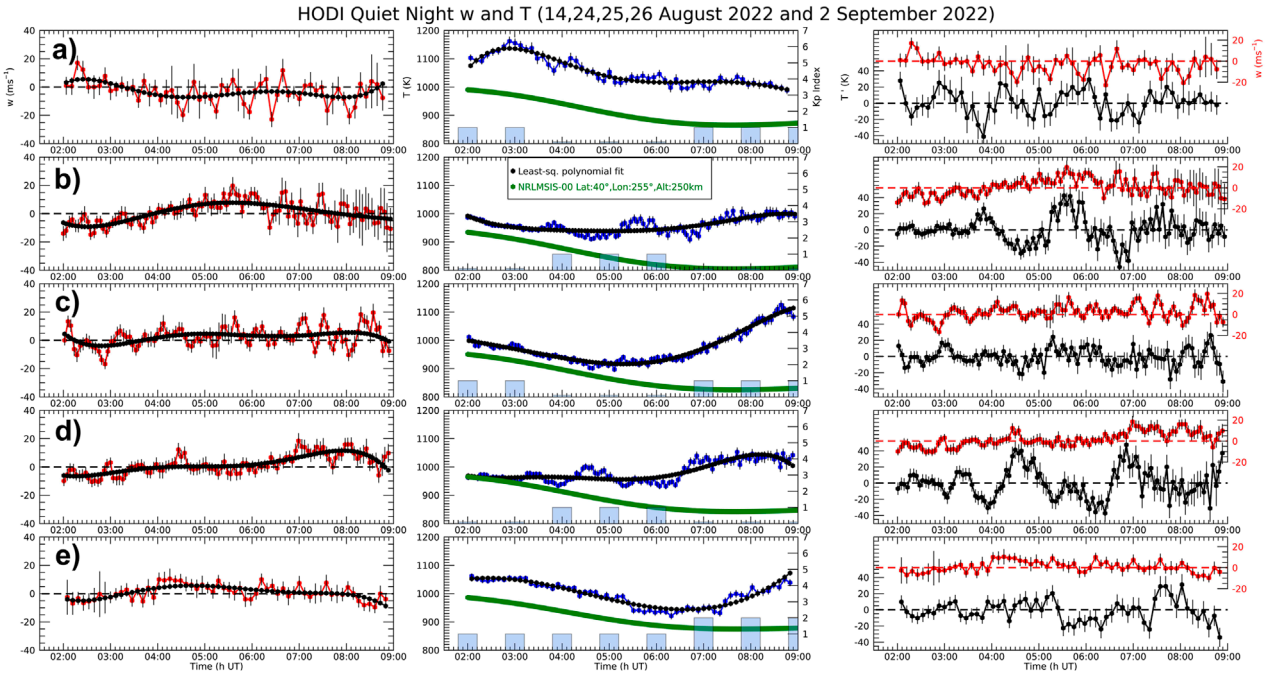

FIGURE 5
Comparison of vertical winds (red, w) and temperature residuals (right black, T ′) measured by HODI derived from the subtraction of observed temperatures (middle blue, T) from the least-square polynomial fitting (middle black) for the dates: **(a)** 14 August 2022, **(b)** 24 August 2022, **(c)** 25 August 2022, **(d)** 26 August 2022, **(e)** 2 September 2022. Temperatures are plotted with the NRLMSIS-00 empirical model with inputs of altitude: 250 km, Lat.:40°, Long.: 255° (bottom green, T) and approximate Kp index (bar graph).

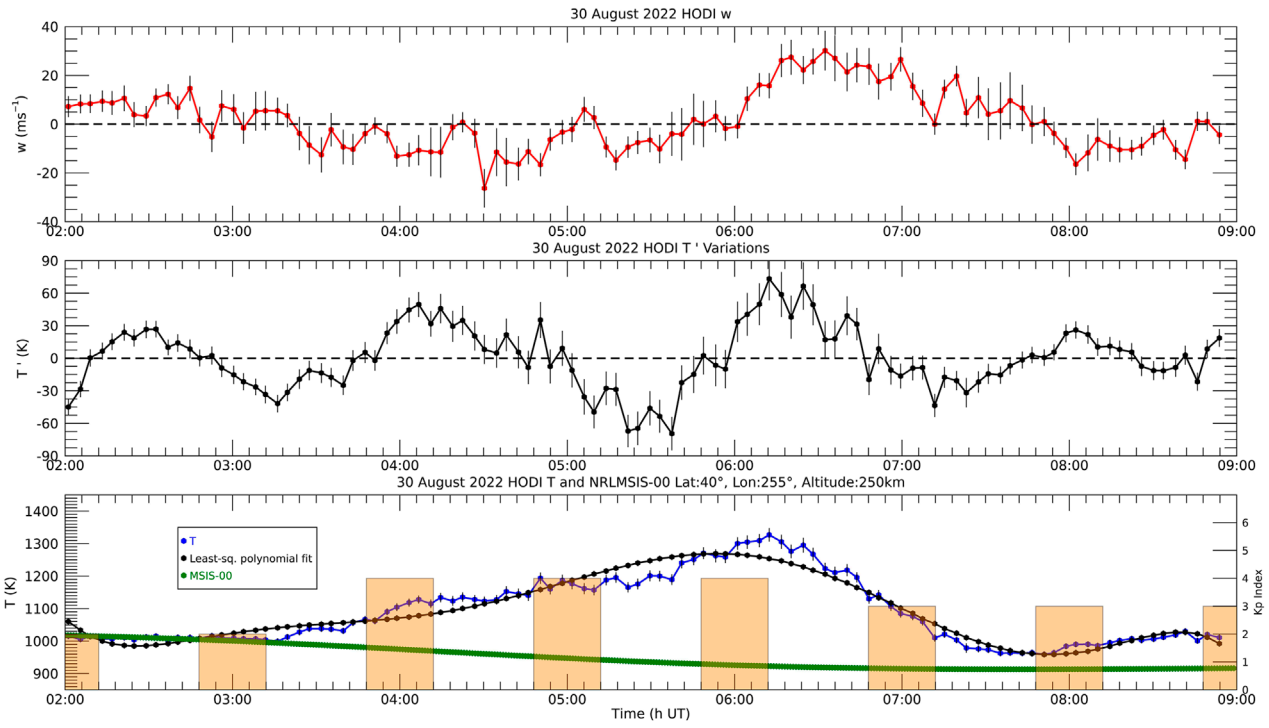

FIGURE 6
HODI observations of vertical winds (top, w) and residual temperatures (middle, T ′) derived from the subtraction of the observed temperatures (bottom blue, T) from the high order least-square polynomial fitting (bottom black) with the NRLMSIS-00 empirical model with inputs of altitude: 250 km, Lat.:40°, Long.: 255° (bottom green, T) and approximate Kp index (bar graph).

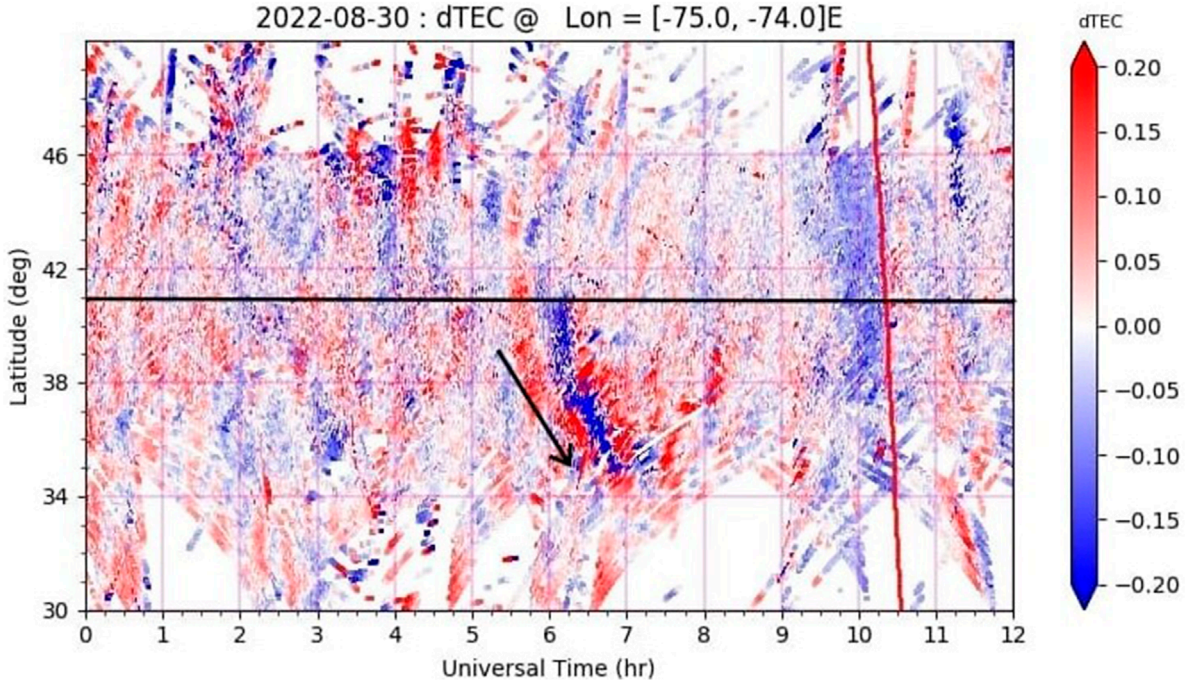

FIGURE 7
dTEC between −75° and −74° east longitude for approximate location of JO (41.03°N, 74.83°W) with varying latitudes and times on 30 August 2022 with a horizontal black line at 41°N. Tilted vertical red line represents the sunrise terminator. The black arrow indicates direction of propagation in the meridional direction.

A keogram (composite of meridional cross-sections) was utilized to examine the dTEC of the approximate location of JO (41.03°N, 74.83°W) changing with time on 30 August 2022 in Figure 7. There is seen an apparent change in dTEC from 0.20 to −0.20 back to 0.20 TEC units around 06:00–07:00 UT, we take this variation to be indicative of a TID that is traveling past the region of ≈41°N latitude. Examining temporal changes in dTEC indicated that a signature of an TID was traveling southwestward, which is the direction expected for such phenomena (Shiokawa et al., 2009; Otsuka et al., 2013; Martinis et al., 2009).

3.2.2 26 August 2022 quiet wind and temperature wave structures

One night of interest from the quiet geomagnetic and clear nights is 26 August 2022 as shown in Figure 8. HODI observed an oscillation in the temperature residuals with an ≈2 hour period and amplitudes of ≈ ±40*K* around 04:00 to 08:00 UT. The repeated wave structure in the temperature residuals suggests the occurrence of a wave train with a period of ≈2 hours. This was seen in conjunction with a low frequency structure with small amplitudes relative to nights with active geomagnetic conditions in the vertical wind data with no discernible qualities relative to amplitude or period. 26 August 2022 had a small increase in raw temperatures from 02:00 to 09:00 UT, indicative of a geomagnetic quiet night at JO. The amplitudes for these wave structures are also larger than their respective errors at time of fluctuation.

A keogram was utilized to examine the dTEC of the approximate location of JO (41.03°N, 74.83°W) changing with time on 26 August 2022 in Figure 9. Some small spatial structures can be seen around 03:30–06:00 UT near −75°E longitude which is directly over JO. This activity and structure in dTEC is indicative with westward and poleward TID propagation based on visual analysis of keograms plotted against latitude and longitude, but the activity and structure are not as perceptible as the TID apparent in the 30 August 2022 keogram in Figure 7.

4 Discussion

The HODI first-light campaign proved to be successful in observing thermospheric wave structures. In every night of observations in the case study, oscillations and GW-like events occurred, irrespective of the degree of geomagnetic activity. For each case night, varying scales of TID activity were also apparent via dTEC keograms.

Observations on 30 August 2022 and 26 August 2022 as shown in Figures 6, 8, respectively, show that a close correlation between vertical wind and temperature fluctuations is not always prevalent, but all feature a series of corresponding oscillations with amplitudes less than a few meters per second but with multiple cycles evident each night. 30 August 2022 shows a low frequency oscillation in the vertical wind and wave train in temperatures potentially associated with a passing TID, while 26 August 2022 shows similar trends in oscillations during a quiet night, with dTEC activity implying propagating TIDs with less discernible structure. The 30 August 2022 night of observation was of particular interest as it was an active night with a large temperature peak near 07:00 UT and vertical wind and temperature oscillations. After visually comparing the dTEC

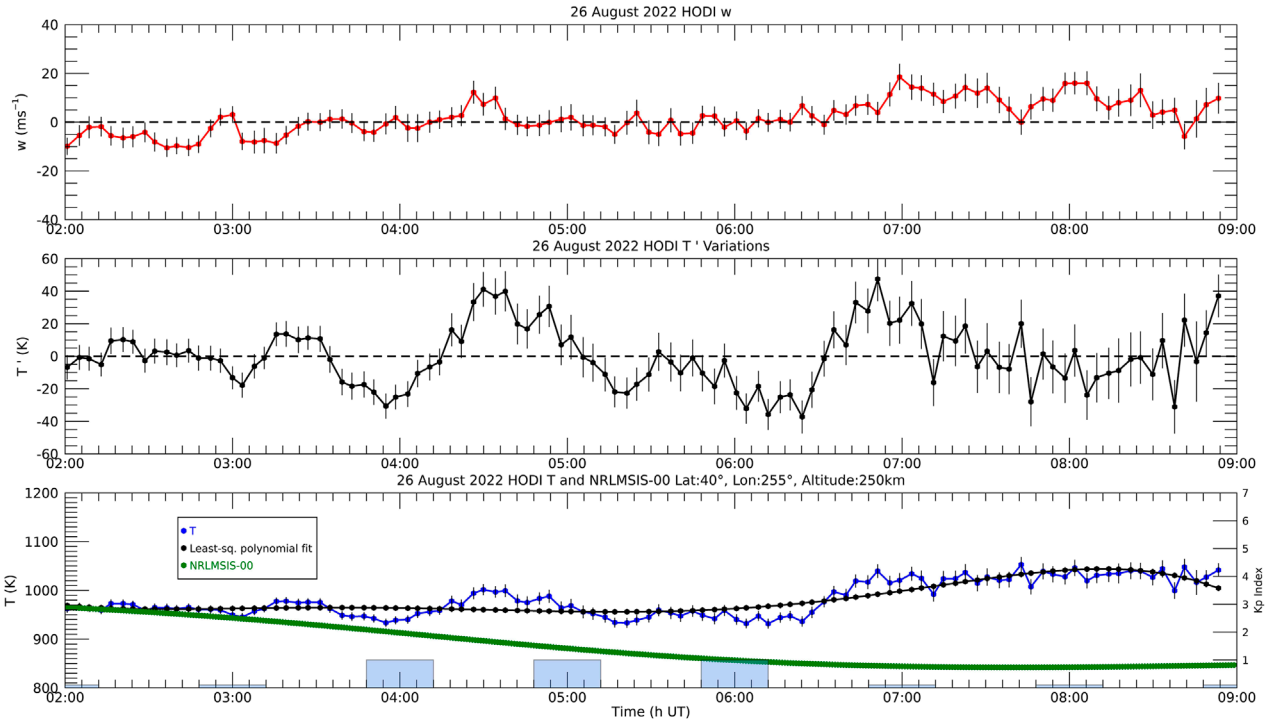

FIGURE 8
HODI observations of vertical winds (top, w) and residual temperatures (middle, T ′) derived from the subtraction of the observed temperatures (bottom blue, T) from the high order least-square polynomial fitting (bottom black) with the NRLMSIS-00 empirical model with inputs of altitude: 250 km, Lat.:40°, Long.: 255° (bottom green, T) and approximate Kp index (bar graph).

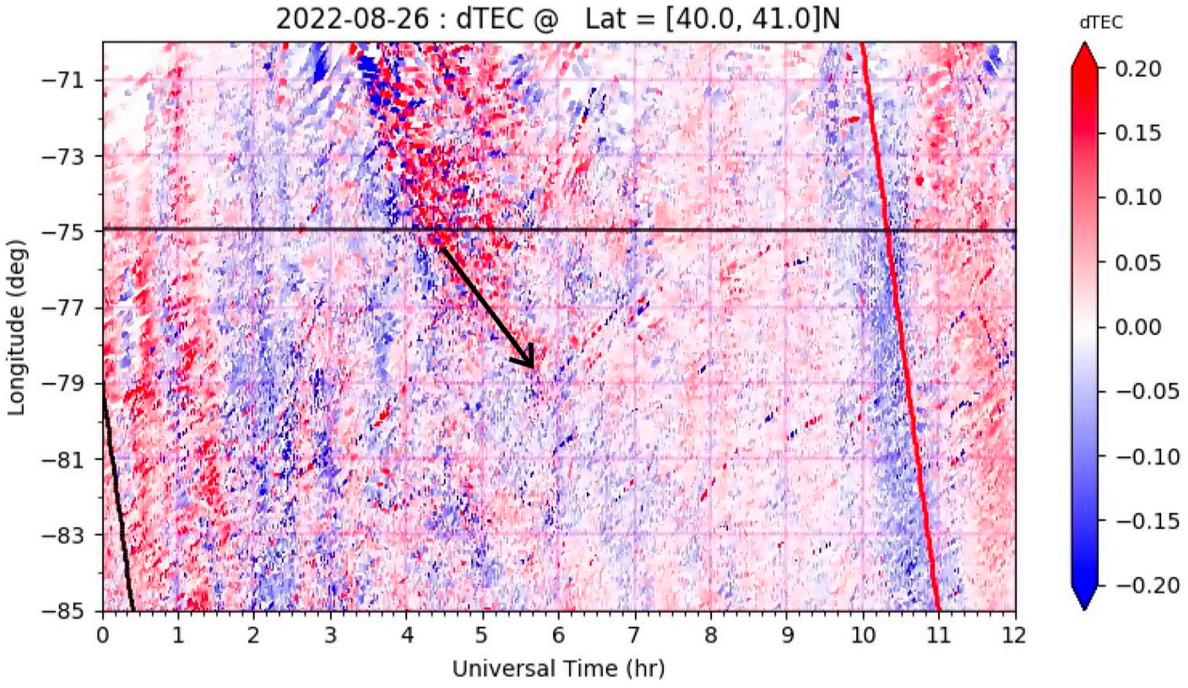

FIGURE 9
dTEC between 40° and 41° north latitude for approximate location of JO (41.03°N, 74.83°W) with varying latitudes and times on 26 August 2022 with a horizontal black line at −75°E. Tilted vertical black and red lines represent the sunset and sunrise terminators, respectively. The black arrow indicates direction of propagation in the zonal direction.

signature of the TID in the 30 August 2022 keogram from Figure 7 and the flows in vertical wind from HODI in Figure 6, it is apparent that the depletion in dTEC does compare well with the vertical wind upward flows observed by HODI. Heating at low altitudes can cause neutral upwelling as well as GWs. This process is well known at auroral latitudes, however, at midlatitudes some processes can provide similar heating effects, such as subauroral polarization streams (SAPS). As a result, an upwelling of vertical winds can normally cause O/N_2 depletion which could explain the depletion in observed dTEC. SAPS heating has been reported in previous studies such as Zhang et al. (2017b). Guo et al. (2018) simulated the GWs excited at subauroral latitudes through SAPS.

Examination of these case study results show that during periods of active geomagnetic conditions, wave structure is prevalent in temperature and often accompanied by long term periodic behavior in the vertical wind. During quiet geomagnetic conditions, wave structure is also prevalent in the temperature and wind data, but with decreased amplitudes. Namely, we observed vertical wind activity to be more vigorous for periods of greater geomagnetic activity. In general, no connection was apparent between temperature and vertical winds except for the one case of what looks to be a monochromatic wave event on 25 July 2022, based on Figure 2 which showcases a near ≈90° phase difference between vertical winds and temperatures to be inferred, as per standard GW polarization relations with slight viscous dissipation (Vadas and Nicolls, 2012). Minor elevated dTEC values were visible during the period of the potential monochromatic GW event, with background poleward propagating TIDs apparent throughout most of the night as shown in Figure 3. Because of the scattered structure during the wave activity in the vertical winds, one-to-one comparisons are indeterminate and dTEC plots are used as an insight into the ionospheric activity at the time of the potential monochromatic GW event. One possible explanation is that the wave structure evident in HODI observations and the dTEC are incongruent because the plasma related to dTEC structure is elevated in altitude relative to the redline 630 nm layer. We suggest that HODI is observing wave structures below the F-2 layer rather than what is within the F-2 layer plasma structure or was dissipated and attenuated prior to observability in the F-2 layer by dTEC observations.

It is possible that HODI observed multiple superimposed GW events, which would make a connection between vertical wind and temperature wave activity nearly impossible to visualize. It is not clear how this superposition will be manifested, but what may be happening is that the high frequency content of the temperature data is converted into a low frequency wave structure by the superposition of GW events with different phases, and the temperature superposition would be additive. This may explain why the temperature wave structure is highly prominent in nights such as 30 and 26 August 2022. Due to this mixing, it would be difficult to quantify exactly how many nights GW behavior was apparent, but we expect these events to appear quite frequently. This behavior may also be seen for the superposition of wind velocities, but because the vertical wind is a vector quantity, this filtering of high frequency content would result in a low frequency wave in vertical winds that is no longer closely correlated with the temperature wave, based on visual inspection. Because this blending of multiple GW events takes place differently for the temperature and wind components, there is no reason to expect a correlation to appear. There is also the consideration that these observations of wind and temperature behavior in the zenith represent an average over the vertical extent of 50–70 km which is the typical range of the OI volume emission profile centered at 240–250 km. The background temperature profile will vary by 5–10 % over this range, which may affect the determination of the residual temperature fluctuations as a result of the filtering of high frequency content caused by the superposition of multiple GW events. We note that the lack of agreement between the vertical wind and temperature variables will certainly be the case for multiple GW events with different phase speeds and different vertical wavelengths.

The viscosity of the thermosphere allows for the absorption of energy from GWs as a result of the transfer of waves from below to the thermosphere medium, but the proportion of energy transfer to the thermosphere from below and the energy transfer from mid to high latitudes have not undergone adequate study. Figure 2 showcases a case of thermospheric viscous dissipation of a potential monochromatic GW event as described by Pitteway and Hines (1963); Nicolls et al. (2012); Vadas and Nicolls (2012) among others. Instruments such as HODI are needed to make progress on understanding the detailed composition of the energy budget in terms of GW transfer, solar heating, and Joule heating that come about as a result of frictional heating due to the interaction of neutral transport with plasma drifts and momentum transfer.

As discussed in Section 2, the possible OH spectral contamination is an important caveat to consider within these results. More observations are needed to further examine these phenomena with greater statistical coverage and further consideration into potential OH contamination. New thermospheric 630 nm emission observations will be obtained with MaxFPI, a novel 20 cm aperture FPI instrument undergoing construction by Keo Scientific which will have ≈8 times greater sensitivity for 630.0 nm observations of vertical winds and narrower prefilter to eliminate OH contamination. First light for this instrument at JO is expected to be during Summer 2025.

5 Conclusion

We have presented the first set of findings from the Hot Oxygen Doppler Imager first light campaign at Jeffer Observatory located in northwestern New Jersey. With the heightened sensitivity of its 15 cm aperture etalon, HODI is able to resolve wave activity in the neutral thermospheric vertical winds and temperature residuals with uncertainties of approximately 3–5 m s^{-1} for vertical wind speeds and 10–15 K for temperatures for 2-min exposures. HODI case study observations for periods of quiet and active geomagnetic activity indicate that vertical wind activity is more vigorous for periods of greater geomagnetic activity. Vertical wind oscillations did not generally have a temperature equivalent except in one case of what looks to be a monochromatic wave event with an associated ≈90° phase lag of vertical winds relative to temperature oscillations with weak viscous dissipation. We have discussed the potential that HODI observed the superposition of multiple GW events as an interpretation of these results, noting the importance of the breadth of the 630 nm volume emission profile in

affecting the blending of multiple GW events. We have also discussed thermosphere/ionosphere interactions between GWs and TIDs by comparing the fluctuations seen in both the FPI and dTEC observations. When conditions are geomagnetically active, there is indeed more wave activity seen in the FPI data that may be related to the increased structural details evident in the dTEC maps. However, even for quiet geomagnetic activity, the FPI data show significant signs of wave fluctuation activity. We suggest that this is an indication of significant GW propagation from the lower atmosphere into the thermosphere. Finally, we plan to revisit these findings using a new FPI instrument, named MaxFPI, that should have a sensitivity gain relative to HODI by nearly an order of magnitude. The MaxFPI prefilters will eliminate any concern regarding OH contamination in the 630 nm OI observations.

Data availability statement

The raw data supporting the conclusions of this article will be made available by the authors, without undue reservation.

Author contributions

AS: Methodology, Writing – review and editing, Writing – original draft, Visualization. JM: Supervision, Conceptualization, Data curation, Writing – review and editing, Investigation. MC: Writing – review and editing, Data curation. AG: Conceptualization, Writing – review and editing, Resources, Investigation, Supervision, Data curation. LG: Conceptualization, Writing – review and editing. S-RZ: Visualization, Methodology, Writing – review and editing. YY: Visualization, Writing – review and editing.

Funding

The author(s) declare that financial support was received for the research and/or publication of this article. NJIT authors recognize support from NSF Grant AGS-2230439. TEC data processing and Madrigal database system are provided to the community by MIT under NSF Grant AGS-1952737 support. Work at MIT is also supported by 80NSSC21K1310 and 80NSSC22K1074, and AGS-2149698, and AGS-2437054.

Acknowledgments

We are pleased to acknowledge the efforts and support of Gilbert Jeffer, Chris Callie, and the United Astronomy Clubs of New Jersey to help achieve the deployment of the HODI instrument to the Jeffer Observatory in Jenny Jump State Forest to obtain the observations described in this report. We would also like to acknowledge funds from the New Jersey Institute of Technology Center for Solar-Terrestrial Research.

Conflict of interest

Author MC was employed by Orion Space Solutions.

The remaining authors declare that the research was conducted in the absence of any commercial or financial relationships that could be construed as a potential conflict of interest.

The author(s) declared that they were an editorial board member of Frontiers, at the time of submission. This had no impact on the peer review process and the final decision.

Generative AI statement

The author(s) declare that no Generative AI was used in the creation of this manuscript.

Publisher's note

References

Armstrong, E. (1969). Doppler shifts in the wavelength of the OI λ6300 line in the night airglow. *Planet. Space Sci.* 17, 957–974. doi:10.1016/0032-0633(69)90101-9

Biondi, M. A., and Feibelman, W. A. (1968). Twilight and nightglow spectral line shapes of oxygen λ6300 and λ5577 radiation. *Planet. Space Sci.* 16, 431–443. doi:10.1016/0032-0633(68)90158-X

Coakley, M. M. (1995). *Application of the CCD Fabry-Perot annular summing technique to thermospheric.* The University of Wisconsin - Madison. Copyright - Database copyright ProQuest LLC; ProQuest does not claim copyright in the individual underlying works.

Ford, E. A. K., Aruliah, A. L., Griffin, E. M., and McWhirter, I. (2007). High time resolution measurements of the thermosphere from Fabry-Perot interferometer measurements of atomic oxygen. *Ann. Geophys.* 25, 1269–1278. doi:10.5194/angeo-25-1269-2007

Guo, J.-P., Deng, Y., Zhang, D.-H., Lu, Y., Sheng, C., and Zhang, S.-R. (2018). The effect of subauroral polarization streams on ionosphere and thermosphere during the 2015 st. patrick's day storm: global ionosphere-thermosphere model simulations. *J. Geophys. Res. Space Phys.* 123, 2241–2256. doi:10.1002/2017JA024781

Harding, B. J., Gehrels, T. W., and Makela, J. J. (2014). Nonlinear regression method for estimating neutral wind and temperature from Fabry-Perot interferometer data. *Appl. Opt.* 53, 666–673. doi:10.1364/AO.53.000666

Hays, P. B., Nagy, A. F., and Roble, R. G. (1969). Interferometric measurements of the 6300 a Doppler temperature during a magnetic storm. *J. Geophys. Res. (1896-1977)* 74, 4162–4168. doi:10.1029/JA074i016p04162

Hernandez, G. (1982). Vertical motions of the neutral thermosphere at midlatitude. *Geophys. Res. Lett.* 9, 555–557. doi:10.1029/GL009i005p00555

Hernandez, G. (1986). *Fabry-Perot interferometers: cambridge studies in modern optics 3*. Cambridge University Press.

Hines, C. O. (1960). Internal atmospheric gravity waves at ionospheric heights. *Can. J. Phys.* 38, 1441–1481. doi:10.1139/p60-150

Huang, C.-S., Miller, C. A., and Kelley, M. C. (1994). Basic properties and gravity wave initiation of the midlatitude F region instability. *Radio Sci.* 29, 395–405. doi:10.1029/93RS01669

Innis, J., Greet, P., Murphy, D., Conde, M., and Dyson, P. (1999). A large vertical wind in the thermosphere at the auroral oval/polar cap boundary seen simultaneously from Mawson and Davis, Antarctica. *J. Atmos. Solar-Terrestrial Phys.* 61, 1047–1058. doi:10.1016/S1364-6826(99)00060-7

Innis, J. L., and Conde, M. (2001). Thermospheric vertical wind activity maps derived from Dynamics Explorer-2 Wats observations. *Geophys. Res. Lett.* 28, 3847–3850. doi:10.1029/2001GL013704

Kelley, M. C., and Fukao, S. (1991). Turbulent upwelling of the mid-latitude ionosphere: 2. theoretical framework. *J. Geophys. Res. Space Phys.* 96, 3747–3753. doi:10.1029/90JA02252

Kelley, M. C., and Makela, J. J. (2001). Resolution of the discrepancy between experiment and theory of midlatitude F-region structures. *Geophys. Res. Lett.* 28, 2589–2592. doi:10.1029/2000GL012777

Kerr, R. B., Kapali, S., Harding, B. J., Riccobono, J., Migliozzi, M. A., Souza, J. R., et al. (2023). Spectral contamination of the 6300Å emission in single-etalon Fabry-Perot interferometers. *J. Geophys. Res. Space Phys.* 128, e2023JA031601. doi:10.1029/2023JA031601

Larsen, M. F., and Meriwether, J. W. (2012). Vertical winds in the thermosphere. *J. Geophys. Res. Space Phys.* 117. doi:10.1029/2012JA017843

Makela, J. J., and Otsuka, Y. (2012). Overview of nighttime ionospheric instabilities at low- and mid-latitudes: coupling aspects resulting in structuring at the mesoscale. *Space Sci. Rev.* 168, 419–440. doi:10.1007/s11214-011-9816-6

Martinis, C., Baumgardner, J., Mendillo, M., Su, S.-Y., and Aponte, N. (2009). Brightening of 630.0 nm equatorial spread-F airglow depletions. *J. Geophys. Res. Space Phys.* 114. doi:10.1029/2008JA013931

Matzka, J., Bronkalla, O., Tornow, K., Elger, K., and Stolle, C. (2021). Geomagnetic Kp index. doi:10.5880/Kp.0001

Meriwether, J. W., Makela, J. J., Huang, Y., Fisher, D. J., Buriti, R. A., Medeiros, A. F., et al. (2011). Climatology of the nighttime equatorial thermospheric winds and temperatures over Brazil near solar minimum. *J. Geophys. Res. Space Phys.* 116. doi:10.1029/2011JA016477

Nicolls, M. J., and Kelley, M. C. (2005). Strong evidence for gravity wave seeding of an ionospheric plasma instability. *Geophys. Res. Lett.* 32. doi:10.1029/2004GL020737

Nicolls, M. J., Vadas, S. L., Meriwether, J. W., Conde, M. G., and Hampton, D. (2012). The phases and amplitudes of gravity waves propagating and dissipating in the thermosphere: application to measurements over Alaska. *J. Geophys. Res. Space Phys.* 117. doi:10.1029/2012JA017542

Otsuka, Y., Suzuki, K., Nakagawa, S., Nishioka, M., Shiokawa, K., and Tsugawa, T. (2013). GPS observations of medium-scale traveling ionospheric disturbances over Europe. *Ann. Geophys.* 31, 163–172. doi:10.5194/angeo-31-163-2013

Perkins, F. (1973). Spread F and ionospheric currents. *J. Geophys. Res. (1896-1977)* 78, 218–226. doi:10.1029/JA078i001p00218

Picone, J. M., Hedin, A. E., Drob, D. P., and Aikin, A. C. (2002). NRLMSISE-00 empirical model of the atmosphere: statistical comparisons and scientific issues. *J. Geophys. Res. Space Phys.* 107, 15–16. doi:10.1029/2002JA009430

Pitteway, M. L. V., and Hines, C. O. (1963). The viscous damping of atmospheric gravity waves. *Can. J. Phys.* 41, 1935–1948. doi:10.1139/p63-194

Shiokawa, K., Otsuka, Y., Ihara, C., Ogawa, T., and Rich, F. J. (2003). Ground and satellite observations of nighttime medium-scale traveling ionospheric disturbance at midlatitude. *J. Geophys. Res. Space Phys.* 108. doi:10.1029/2002JA009639

Shiokawa, K., Otsuka, Y., and Ogawa, T. (2009). Propagation characteristics of nighttime mesospheric and thermospheric waves observed by optical mesosphere thermosphere imagers at middle and low latitudes. *Earth, Planets Space* 61, 479–491. doi:10.1186/bf03353165

Shiokawa, K., Otsuka, Y., Oyama, S., Nozawa, S., Satoh, M., Katoh, Y., et al. (2012). Development of low-cost sky-scanning Fabry-Perot interferometers for airglow and auroral studies. *Earth, Planets Space* 64, 1033–1046. doi:10.5047/eps.2012.05.004

Sipler, D., Biondi, M., and Zipf, M. (1995). Vertical winds in the midlatitude thermosphere from Fabry-Perot interferometer measurements. *J. Atmos. Terr. Phys.* 57, 621–629. doi:10.1016/0021-9169(94)00102-T

Trinh, Q. T., Ern, M., Doornbos, E., Preusse, P., and Riese, M. (2018). Satellite observations of middle atmosphere–thermosphere vertical coupling by gravity waves. *Ann. Geophys.* 36, 425–444. doi:10.5194/angeo-36-425-2018

Unick, C., Trondsen, T., Wyatt, D., and Meriwether, J. (2019). An apochromatic lens based Fabry-Pérot interferometer for accurate measurements of lower thermospheric neutral wind velocity and temperature. *AGU Fall Meet. Abstr.* 2019, SA33B–3155.

Vadas, S. L., and Nicolls, M. J. (2012). The phases and amplitudes of gravity waves propagating and dissipating in the thermosphere: theory. *J. Geophys. Res. Space Phys.* 117. doi:10.1029/2011JA017426

Zhang, S.-R., Erickson, P. J., Gasque, L. C., Aa, E., Rideout, W., Vierinen, J., et al. (2021). Electrified postsunrise ionospheric perturbations at Millstone Hill. *Geophys. Res. Lett.* 48, e2021GL095151. doi:10.1029/2021GL095151

Zhang, S.-R., Erickson, P. J., Goncharenko, L. P., Coster, A. J., Rideout, W., and Vierinen, J. (2017a). Ionospheric bow waves and perturbations induced by the 21 august 2017 solar eclipse. *Geophys. Res. Lett.* 44 (12), 067–12,073. doi:10.1002/2017GL076054

Zhang, S.-R., Erickson, P. J., Zhang, Y., Wang, W., Huang, C., Coster, A. J., et al. (2017b). Observations of ion-neutral coupling associated with strong electrodynamic disturbances during the 2015 St. Patrick's Day storm. *J. Geophys. Res. Space Phys.* 122, 1314–1337. doi:10.1002/2016JA023307

Zhang, S.-R., Zhang, Y., Wang, W., and Verkhoglyadova, O. P. (2017c). Geospace system responses to the St. Patrick's Day storms in 2013 and 2015. *J. Geophys. Res. Space Phys.* 122, 6901–6906. doi:10.1002/2017JA024232